

# Effects of parallel dynamics on vortex structures in electron temperature gradient driven turbulence

M. Nakata,<sup>1,a)</sup> T.-H. Watanabe,<sup>1,2</sup> H. Sugama,<sup>2</sup> and W. Horton<sup>3</sup>

<sup>1</sup>*The Graduate University for Advanced Studies, Toki, Gifu 509-5292, Japan*

<sup>2</sup>*National Institute for Fusion Science, Toki, Gifu 509-5292, Japan*

<sup>3</sup>*Institute for Fusion Studies, The University of Texas at Austin, Austin, Texas 78712, USA*

(Received 7 November 2010; accepted 17 December 2010; published online 10 January 2011)

Vortex structures and related heat transport properties in slab electron temperature gradient (ETG) driven turbulence are comprehensively investigated by means of nonlinear gyrokinetic Vlasov simulations, with the aim of elucidating the underlying physical mechanisms of the transition from turbulent to coherent states. Numerical results show three different types of vortex structures, i.e., coherent vortex streets accompanied with the transport reduction, turbulent vortices with steady transport, and a zonal-flow-dominated state, depending on the relative magnitude of the parallel compression to the diamagnetic drift. In particular, the formation of coherent vortex streets is correlated with the strong generation of zonal flows for the cases with weak parallel compression, even though the maximum growth rate of linear ETG modes is relatively large. The zonal flow generation in the ETG turbulence is investigated by the modulational instability analysis with a truncated fluid model, where the parallel dynamics such as acoustic modes for electrons is incorporated. The modulational instability for zonal flows is found to be stabilized by the effect of the finite parallel compression. The theoretical analysis qualitatively agrees with secondary growth of zonal flows found in the slab ETG turbulence simulations, where the transition of vortex structures is observed. © 2011 American Institute of Physics. [doi:10.1063/1.3535584]

## I. INTRODUCTION

Microscale turbulence driven by drift wave instabilities has extensively been studied in order to elucidate mechanisms of anomalous transport of particle, momentum, and heat in magnetically confined plasmas.<sup>1</sup> A number of works have been dedicated so far to gyrokinetic and gyrofluid simulations of ion temperature gradient (ITG) driven turbulence, where a spontaneous generation of zonal flows regulating the ion heat transport has been revealed.<sup>2–9</sup> Zonal flows with the radial scale length of the ion gyroradius have also been observed experimentally by a direct measurement of electrostatic potential fluctuations.<sup>10</sup>

Electron temperature gradient (ETG) modes and/or trapped electron modes are more recently investigated theoretically and numerically as a main cause of the anomalous electron heat transport.<sup>11–20</sup> Since the perpendicular gyromotion of ambient ions with large gyroradii shields the zonal component of potential fluctuations, the zonal flow generation and the resultant turbulence suppression are weaker than those in the ITG case.<sup>21,22</sup> Thus, the ETG turbulence inherently involves various vortex structures, such as turbulent vortices, zonal flows, and radially elongated streamers, which strongly depend on geometrical and plasma parameters. Especially, the nonlinear dynamics of streamers, which may lead to substantial enhancement of the heat transport in toroidal systems, has been actively pursued.<sup>11,13–15,18</sup> From the aspect of turbulence control with regulating the heat transport in the future fusion plasmas, it is worthwhile to understand fundamental physics behind the formation of

vortex structures including zonal flows and its stability, as well as the related transport properties.

In our earlier work,<sup>23</sup> we have investigated vortex structures in the slab ETG turbulence as well as velocity-space structures of the distribution function by means of the gyrokinetic Vlasov simulations with high phase-space resolution and have found the formation of coherent vortex streets accompanied with the significant transport reduction in the nonlinear phase. Detailed analysis of the distribution function clarified that the transport reduction is associated with the phase matching between the potential and temperature fluctuations rather than the reduction of the fluctuation amplitude. Furthermore, we have revealed that a traveling wave solution of a Hasegawa–Mima type equation derived from the gyrokinetic equation for electrons describes well the coherent vortex streets found in the turbulence simulation.

In the present paper, a comprehensive parameter study of the slab ETG turbulence is carried out by means of the nonlinear gyrokinetic Vlasov simulations, with the aim of elucidating underlying physical mechanisms of the transition of vortex structures from turbulent to coherent ones and the related transport reduction. Especially, the dependence on the magnitude of the parallel compression, which causes couplings with the higher-order fluid moments, and the electron temperature gradient is intensively examined. The detailed analyses reveal a critical condition of the transition of vortex structures associated with the parallel dynamics and may provide one a useful insight into the turbulence control.

Although the present study is limited to the two-dimensional slab system, it also contributes to a deeper understanding of the toroidal ETG turbulence. Actually, in the

<sup>a)</sup>Electronic mail: nakata.motoki@nifs.ac.jp.

toroidal system with a reversed magnetic shear profile, the effect of the parallel compression becomes more important in a weak magnetic shear region where the magnetic drift frequency decreases and the slab ETG modes may be destabilized as well as the toroidal ones.<sup>17–20</sup>

In the latter part of this paper, we discuss the dependence of zonal flow generation on the magnitude of the parallel compression based on the modulational instability analysis with a truncated fluid model, where the parallel dynamics such as acoustic modes due to the electron inertia is taken into account. This is an extension of the conventional modulational instability analysis by means of the Hasegawa–Mima type model.<sup>19,24–27</sup>

The remainder of this paper is organized as follows. A simulation model used in the present study is described in Sec. II. Nonlinear simulation results of the slab ETG turbulence are presented in Sec. III. Then, we discuss in detail the transition of vortex structures, which is closely associated with the zonal flow generation, as well as the related transport properties. In order to find qualitative understanding of the transition of vortex structures, the modulational instability analysis is carried out in Sec. IV, where the dependence of the zonal flow growth rate on the magnitude of the parallel compression is compared with the turbulence simulation results. Finally, concluding remarks on the present study are given in Sec. V.

## II. SIMULATION MODEL AND LINEAR ANALYSIS

A gyrokinetic model considered here is the same as that used in a previous work on slab ETG/ITG turbulence simulations.<sup>23</sup> Time evolution of the perturbed gyrocenter distribution function  $\delta f_{k_{\perp}}^{(g)}$  is numerically solved, where the equilibrium part is assumed to be the local Maxwellian. Also, we assume that  $v_{\perp}$ -dependence of  $\delta f_{k_{\perp}}^{(g)}$  is given by the local Maxwellian, i.e.,  $\delta f_{k_{\perp}}^{(g)}(v_{\perp}, u_{\parallel}, t) = F_{M\perp}(v_{\perp}) \delta f_{k_{\perp}}(u_{\parallel}, t)$ , where  $F_{M\perp} \equiv (m_e/2\pi T_e) \exp(-m_e v_{\perp}^2/2T_e)$ . This treatment enables us to keep high resolution in the wave number and the  $u_{\parallel}$ -space and then the fine-scale structures of the distribution function are accurately resolved as well as the turbulent vortices. A periodic two-dimensional slab configuration with a uniform magnetic field is considered in the present study, where the plasma is assumed to be homogeneous in the  $z$ -direction. The magnetic field  $\mathbf{B}$  is set in the  $y$ - $z$  plane such that  $\mathbf{B} = B(\mathbf{e}_z \cos \theta + \mathbf{e}_y \sin \theta) \approx B(\mathbf{e}_z + \theta \mathbf{e}_y)$  for  $\theta \ll 1$ , where  $\{\mathbf{e}_x, \mathbf{e}_y, \mathbf{e}_z\}$  and  $\theta$  denote the unit basis vectors in a local Cartesian coordinate system and the tilt angle of field lines, respectively. The  $x$ -,  $y$ -, and  $z$ -directions considered here correspond to the radial, poloidal, and toroidal directions in a toroidal system, respectively. Neglecting the parallel nonlinearity on the gyrokinetic equation<sup>28</sup> and integrating over the  $v_{\perp}$ -space, one obtains the following equation for the perturbed distribution function  $\delta f_{k_{\perp}}(u_{\parallel}, t)$  written in the wave number space:

$$\begin{aligned} & \left( \frac{\partial}{\partial t} + ik_{\parallel} u_{\parallel} \right) \delta f_{k_{\perp}} - \frac{c}{B} \sum_{\Delta} \mathbf{b} \cdot (\mathbf{k}'_{\perp} \times \mathbf{k}''_{\perp}) \delta \psi_{k'_{\perp}} \delta f_{k''_{\perp}} - C_{\parallel}(\delta f_{k_{\perp}}) \\ & = -i \left\{ \omega_{*e} \left[ 1 + \eta_e \left( \frac{m_e v_{\parallel}^2}{2T_e} - \frac{1}{2} - \frac{k_{\perp}^2 \rho_{te}^2}{2} \right) \right] - k_{\parallel} u_{\parallel} \right\} F_{M\parallel} \frac{e \delta \psi_{k_{\perp}}}{T_e}. \end{aligned} \quad (1)$$

Here, the perpendicular wave number vector is given by  $\mathbf{k}_{\perp} = k_x \mathbf{e}_x + k_y \mathbf{e}_y$ . Since  $k_z$  vanishes due to the translational symmetry in the  $z$ -direction, the parallel wave number is reduced to  $k_{\parallel} = \theta k_y$ . The electron thermal gyroradius is defined by  $\rho_{te} \equiv v_{te}/\Omega_e$ , where  $v_{te} \equiv (T_e/m_e)^{1/2}$  and  $\Omega_e \equiv eB/m_e c$  are the electron thermal speed and the electron gyrofrequency, respectively. The gyrophase-averaged potential fluctuation integrated over the  $v_{\perp}$ -space is denoted by  $\delta \psi_{k_{\perp}} \equiv \delta \phi_{k_{\perp}} \exp(-k_{\perp}^2 \rho_{te}^2/2)$ , where  $\delta \phi_{k_{\perp}}$  represents the potential fluctuation evaluated at the particle position. The symbol  $\sum_{\Delta}$  appearing in the nonlinear term of Eq. (1) stands for the summation over Fourier modes which satisfy the triad-interaction condition, i.e.,  $\mathbf{k}_{\perp} = \mathbf{k}'_{\perp} + \mathbf{k}''_{\perp}$ . The background Maxwellian distribution with respect to  $u_{\parallel}$  is denoted by  $F_{M\parallel} \equiv n_0 (m_e/2\pi T_e)^{1/2} \exp(-m_e u_{\parallel}^2/2T_e)$ . Since, in general, the gradient scale lengths of the equilibrium density  $L_n \equiv -(d \ln n_0/dx)^{-1}$  and the equilibrium temperature  $L_T \equiv -(d \ln T_e/dx)^{-1}$  are much longer than scale lengths of the turbulent fluctuations in the direction perpendicular to the magnetic field, we set  $L_n$  and  $L_T$  to be constant here. The inhomogeneities of  $n_0$  and  $T_e$  appear in the electron drift frequency  $\omega_{*e} \equiv (cT_e/eBL_n)k_y = (v_{te}/L_n)k_y \rho_{te}$  and the electron temperature gradient parameter  $\eta_e \equiv L_n/L_T$ . Also, we introduce a dimensionless parameter  $\Theta$  associated with the tilt angle of magnetic field lines ( $\Theta \equiv k_{\parallel} L_T/k_y \rho_{te} = \theta L_T/\rho_{te}$ ). The tilt angle parameter  $\Theta$  reflects the magnitude of the parallel advection (or the parallel compression) term in proportion to  $k_{\parallel}$  and turns out to be an important parameter for the transition of the vortex structures in the slab ETG turbulence as discussed in Sec. III.

A weak collisional effect is introduced in terms of a model collision operator given by  $C_{\parallel}(\delta f_{k_{\perp}}) \equiv \nu_e \partial_{u_{\parallel}} (v_{te}^2 \partial_{u_{\parallel}} + u_{\parallel}) \delta f_{k_{\perp}}$ , where  $\nu_e$  is the electron collision frequency. The collision operator acting on  $\delta f_{k_{\perp}}$  smoothes out the fine-scale fluctuations generated in the  $u_{\parallel}$ -space.

The electrostatic potential fluctuation is determined by the Poisson equation written in the wave number space as follows:

$$\begin{aligned} k_{\perp}^2 \lambda_{De}^2 n_0 \frac{e \delta \phi_{k_{\perp}}}{T_e} & = \left[ \int d\mathbf{v} J_0^i \delta f_{ik_{\perp}}^{(g)} - n_0 \frac{e \delta \phi_{k_{\perp}}}{T_i} (1 - \Gamma_0^i) \right] \\ & - \left[ \int d\mathbf{v} J_0^e \delta f_{ek_{\perp}}^{(g)} + n_0 \frac{e \delta \phi_{k_{\perp}}}{T_e} (1 - \Gamma_0^e) \right], \end{aligned} \quad (2)$$

where  $\lambda_{De} \equiv (T_e/4\pi n_0 e^2)^{1/2}$  is the electron Debye length. The first and the second terms on the right hand side of Eq. (2) denote the ion-particle-density and the electron-particle-density fluctuations represented with the gyrocenter distribution functions, respectively. The factors  $J_0^i$  and  $\Gamma_0^i$  are defined by  $J_0^i \equiv J_0(k_{\perp} v_{\perp}/\Omega_i)$  and  $\Gamma_0^i \equiv I_0(k_{\perp}^2 \rho_{ti}^2) \exp(-k_{\perp}^2 \rho_{ti}^2)$  with the

zeroth-order Bessel and modified-Bessel functions, respectively, where the superscripts and subscripts “s” indicate the particle species for ions and electrons. Characteristic scale lengths of the ETG turbulence are, in general, comparable to the electron thermal gyroradius, which is much shorter than the ion one, i.e.,  $\lambda = 2\pi/k_{\perp} \sim \rho_{te} \ll \rho_{ti}$ . Since  $J_0^i$  and  $\Gamma_0^i$  become negligibly small in the limit of  $k_{\perp}\rho_{ti} \gg 1$ , the ion density response to the potential fluctuation is thus reduced to the adiabatic one. Additionally, we assume that the scale lengths of turbulent fluctuations are longer than the electron Debye length and ignore the term proportional to  $k_{\perp}^2\lambda_{De}^2$  in Eq. (2). These arguments and the integration for  $v_{\perp}$  reduce the Poisson equation described above to the quasineutrality condition with the adiabatic ion response as follows:

$$\int du_{\parallel} \delta f_{ek_{\perp}} = -n_0 \Lambda_{k_{\perp}} \frac{e \delta \psi_{k_{\perp}}}{T_e}, \quad (3)$$

where  $\Lambda_{k_{\perp}} \equiv \exp(k_{\perp}^2 \rho_{te}^2) (1 + \tau - \Gamma_0^e)$  with  $\tau \equiv T_e/T_i$ .

Using the closed set of equations described above, one can derive a balance equation with respect to the entropy variable  $\delta S$  defined by a functional of the distribution function  $\delta f_{k_{\perp}}$ ,

$$\frac{d}{dt} (\delta S + W) = L_T^{-1} Q_e + D, \quad (4)$$

where

$$\delta S \equiv \sum_{k_{\perp}} \int du_{\parallel} \frac{|\delta f_{k_{\perp}}|^2}{2F_{M\parallel}},$$

$$\begin{aligned} W &\equiv \sum_{k_{\perp}} \frac{n_0}{2} [1 + \tau - \Gamma_0^e] \left| \frac{e \delta \phi_{k_{\perp}}}{T_e} \right|^2 \\ &= \sum_{k_{\perp}} \frac{n_0}{2} \Lambda_{k_{\perp}} \left| \frac{e \delta \phi_{k_{\perp}}}{T_e} \right|^2, \end{aligned}$$

$$L_T^{-1} Q_e \equiv L_T^{-1} \sum_{k_{\perp}} \frac{c}{B} \text{Re} \left[ ik_y \delta \psi_{k_{\perp}} \int du_{\parallel} \left( \frac{m_e v_{\parallel}^2}{2T_e} - \frac{1}{2} \right) \delta f_{k_{\perp}}^* \right],$$

and

$$D \equiv \sum_{k_{\perp}} \int du_{\parallel} C_{\parallel}(\delta f_{k_{\perp}}) \frac{\delta f_{k_{\perp}}^*}{F_{M\parallel}}$$

denote the entropy variable, the potential energy, the entropy production due to the turbulent heat flux driven by the electron temperature gradient (thermodynamic force), and the collisional dissipation, respectively. In a statistically steady state of the ETG turbulence, the entropy balance relation indicates that the mean entropy production due to turbulent transport balances with the mean collisional dissipation, i.e.,  $L_T^{-1} \bar{Q}_e = -\bar{D} \geq 0$  (the overline represents the time average in a saturated phase), and provides us a good measure for the accuracy of the turbulence simulation. It is confirmed that for all the turbulence simulation results discussed below, the entropy balance relation is accurately satisfied within an error less than 0.5% of the mean collisional dissipation level.

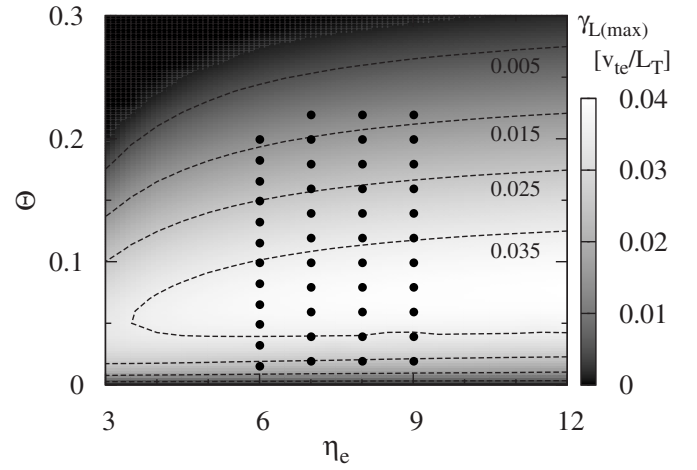


FIG. 1. Contour of the maximum linear growth rate  $\gamma_{L(\max)}$  of linear ETG modes with respect to  $\eta_e$  and  $\Theta$ . Circular symbols represent the parameter sets used in turbulence simulations shown in Sec. III.

The linear growth rate and the real frequency of the ETG modes depend on the collision frequency  $\nu_e$ , the temperature ratio  $\tau$ , the electron temperature gradient parameter  $\eta_e$ , and the tilt angle parameter  $\Theta$ . Using Eqs. (1) and (3), the dispersion relation of the linear ETG mode is given by

$$\begin{aligned} 1 + \Lambda_{k_{\perp}} - \frac{\zeta}{\sqrt{2\Theta}} - \left[ \frac{\zeta^2}{\sqrt{2\Theta}} - \zeta + \frac{1}{\sqrt{2\Theta}} \right. \\ \left. \times \left\{ 1 - \frac{\eta_e}{2} (1 + k_{\perp}^2 \rho_{te}^2) \right\} \right] Z(\zeta) = 0, \end{aligned} \quad (5)$$

where  $\zeta$  is defined as  $\zeta \equiv \omega / \sqrt{2} k_{\parallel} \nu_e$  with a complex frequency  $\omega$ . The plasma dispersion function is denoted by  $Z(\zeta) \equiv i\sqrt{\pi} \exp(-\zeta^2) (1 + \text{Erf}(i\zeta))$  in terms of the error function  $\text{Erf}(z)$ . Since the collision frequency is set to be sufficiently small here ( $\nu_e L_T / \nu_{te} = 2.0 \times 10^{-4}$ ), the effect of the collisionality is neglected in the above dispersion relation. Also, the temperature ratio  $\tau$  is fixed to unity so that the independent physical parameters are  $\eta_e$  and  $\Theta$  in the present study discussed in detail below.

Figure 1 shows the contour of the maximum growth rate of the linear ETG modes  $\gamma_{L(\max)}$  on the two-dimensional  $(\eta_e, \Theta)$ -space. Here, the parameter sets used in the turbulence simulations are also plotted with solid circular symbols. One finds that in the normalization with  $L_T$ , the maximum growth rate  $\gamma_{L(\max)}$  has weak dependence on  $\eta_e$ , whereas it has stronger dependence on  $\Theta$ . From this point of view, we have carried out the parameter scan of the ETG turbulence for  $\eta_e \geq 6$  with focusing on the dependence on  $\Theta$ . In the present parameter study, 45 nonlinear gyrokinetic simulations have been carried out in total [12 runs for  $\eta_e=6$  and 11 runs for  $\eta_e=\{7, 8, 9\}$ ].

The  $k_y$ -spectra of the linear growth rate  $\gamma_L$  for  $\eta_e=6$  are shown in Fig. 2, where  $\Theta = \{0.033, 0.050, 0.133, 0.150, 0.200\}$  are chosen as five representative cases. Here, we set  $k_x=0$  because the finite  $k_x$  has a stabilizing effect. From this figure, one can see that the parameter  $\Theta$  is related to not only the magnitude of the growth rate, but also the width of unstable region in the  $k_y$ -space.

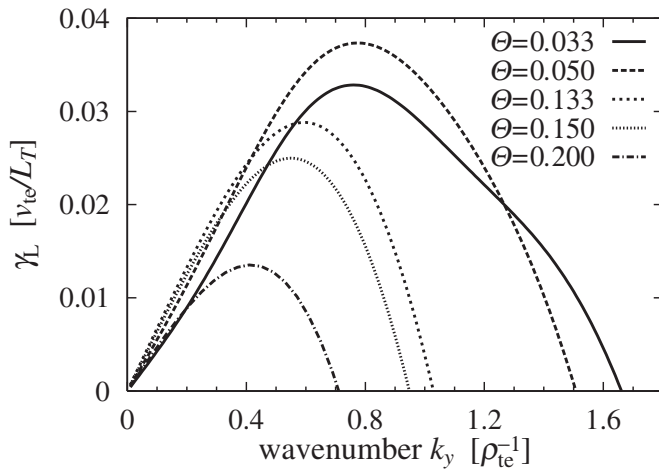


FIG. 2. Growth rates  $\gamma_L$  of linear ETG modes for  $\Theta = \{0.033, 0.050, 0.133, 0.150, 0.200\}$ , where  $\eta_e = 6$  and  $k_x = 0$ .

In the nonlinear gyrokinetic simulations, physical quantities are normalized as  $x = x'/\rho_{te}$ ,  $y = y'/\rho_{te}$ ,  $v_{\parallel} = v'_{\parallel}/v_{te}$ ,  $t = t'v_{te}/L_T$ ,  $v_e = v'_e L_T/v_{te}$ ,  $F_{M\parallel} = F'_{M\parallel} v_{te}/n_0$ ,  $\delta f_{k\perp} = \delta f'_{k\perp} L_T v_{te}/\rho_{te} n_0$  and  $\delta \phi_{k\perp} = e \delta \phi'_{k\perp} L_T / T_e \rho_{te}$ , where the prime means a dimensional quantity. The number of Fourier modes in the two-dimensional wave number space and the grids on the  $v_{\parallel}$ -space are set to be  $(N_{k_x}, N_{k_y}, N_{v_{\parallel}}) = (129, 257, 2049)$ . The range of the wave numbers  $k_x$ ,  $k_y$ , and the  $v_{\parallel}$ -coordinate are  $0 \leq k_x \leq k_{\max}$ ,  $-k_{\max} \leq k_y \leq k_{\max}$ , and  $-v_{\max} \leq v_{\parallel} \leq v_{\max}$  with  $k_{\max} = 12.8$  and  $v_{\max} = 10$ , respectively. The size of the simulation domain is set to be a square with  $L_x = L_y = 20\pi\rho_{te}$  and then the nonzero minimum absolute value of the wave number is  $k_{\min} = 0.1$ . The initial condition for the distribution function is given by the Maxwellian distribution with a small amplitude of  $10^{-6}$  and random phases.

### III. RESULTS OF NONLINEAR GYROKINETIC SIMULATIONS

#### A. Vortex structures and transport properties

Results of the parameter study with respect to  $\eta_e$  and  $\Theta$  on the nonlinear gyrokinetic simulations are shown and discussed here. The results for  $\Theta = \{0.033, 0.050, 0.133, 0.150, 0.200\}$  with  $\eta_e = 6$  are selected as representative cases, where the growth rates of linear ETG modes are shown in Fig. 2. The other cases including the results for  $\eta_e = \{7, 8, 9\}$  are also summarized in Sec. III B.

Figures 3(a) and 3(b) show time evolution of the heat diffusivity  $\chi_e (= Q_e)$  for the representative cases. [Note that  $\chi'_e \equiv Q'_e / (n_0 L_T^{-1})$  is reduced to  $\chi_e = Q_e$  in terms of the normalization with  $L_T$ , where the prime means dimensional quantities.] The initial perturbation linearly grows due to the ETG instability until the nonlinear saturation takes place. Then, one clearly finds the different behavior of  $\chi_e$  depending on the value of  $\Theta$  in nonlinear phases. Transition of the turbulence accompanied with the transport reduction for  $t \geq 1000$  is observed in the cases of  $\Theta = \{0.033, 0.050\}$  [Fig. 3(a)], while the steady transport is sustained in the cases of  $\Theta = \{0.133, 0.150\}$  [Fig. 3(b)]. For the case of  $\Theta = 0.200$  [Fig. 3(b)], we find that the turbulent transport is almost

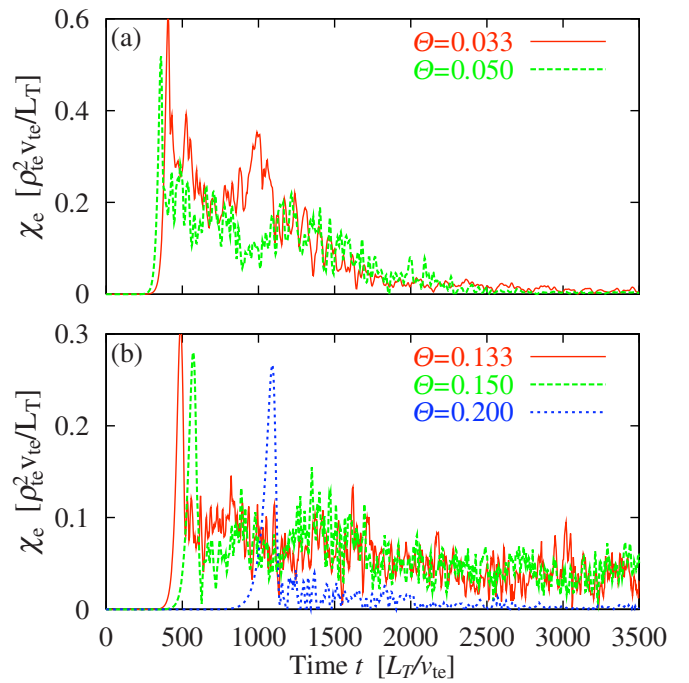


FIG. 3. (Color online) Time evolution of the heat diffusivity  $\chi_e$  for (a)  $\Theta = \{0.033, 0.050\}$  and (b)  $\Theta = \{0.133, 0.150, 0.200\}$ , where  $\eta_e = 6$ .

completely suppressed in the nonlinear phase. The significant suppression of the transport for  $\Theta = 0.200$  is similar to that observed in the ITG turbulence simulations with  $L_T^{-1}$  below the nonlinearly upshifted critical gradient (Dimits shift).<sup>2,3</sup> The heat diffusivity for the above cases are summarized in Table I, where  $\overline{\chi_e^<}$  and  $\overline{\chi_e^>}$  denote the time-averaged values taken for early (immediately after the saturation of linear ETG modes, e.g.,  $500 \leq t \leq 1300$  for  $\Theta = 0.033$ ) and late (e.g.,  $t \leq 2500$ ) nonlinear phases, respectively. Here, the fixed time interval  $\Delta t_{\text{ave}} = 750$  is used for the time averages.

It is expected that the different behavior of the heat diffusivity discussed above is closely related to the zonal flow generation. The time evolution of the zonal flow potential energy normalized by the total one  $W$ , i.e.,  $W_{zf}/W$ , is shown in Figs. 4(a) and 4(b), where  $W_{zf}$  represents the zonal flow component of  $W$ . It should be emphasized that after the initial saturation of the zonal flow growth ( $t \geq 1000$ ), the subsequent generation of the zonal flow to a higher level is found in the cases of  $\Theta = \{0.033, 0.050\}$  [Fig. 4(a)], while the zonal flow amplitude remains almost constant for the other cases [Fig. 4(b)]. The secondary growth of the zonal flow shows the clear correlation with the transport reduction

TABLE I. Time-averaged heat diffusivity in the early and late nonlinear phases.

$\Theta$	$\overline{\chi_e^<} [\rho_{te}^2 v_{te} / L_T]$	$\overline{\chi_e^>} [\rho_{te}^2 v_{te} / L_T]$	Types of evolution
0.033	$1.99 \times 10^{-1}$	$1.01 \times 10^{-2}$	Transitional
0.050	$1.38 \times 10^{-1}$	$3.55 \times 10^{-3}$	Transitional
0.133	$6.37 \times 10^{-2}$	$1.23 \times 10^{-2}$	Steady
0.150	$6.84 \times 10^{-2}$	$2.47 \times 10^{-2}$	Steady
0.200	$1.17 \times 10^{-2}$	$2.29 \times 10^{-3}$	Suppressed

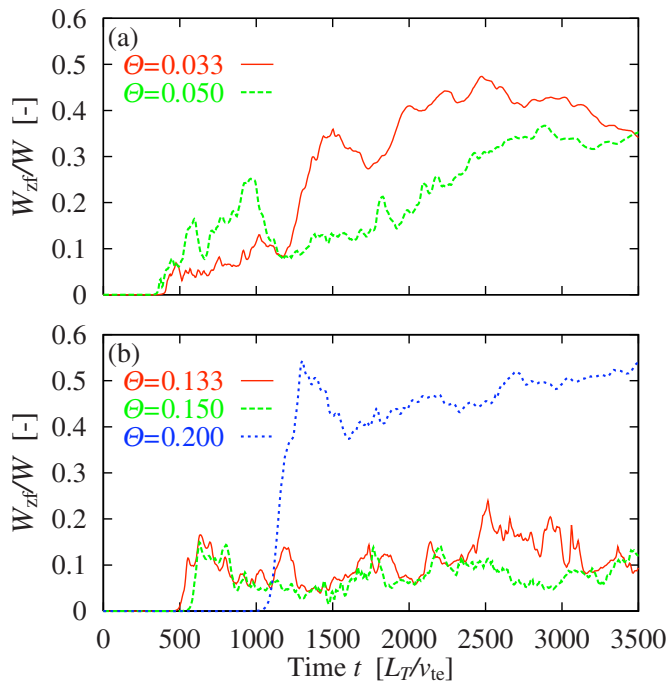


FIG. 4. (Color online) Time evolution of normalized energy of zonal flows  $W_{zf}/W$  for (a)  $\Theta=\{0.033, 0.050\}$  and (b)  $\Theta=\{0.133, 0.150, 0.200\}$ , where  $\eta_e=6$ .

found in the late nonlinear phase, as shown in Fig. 3(a). The other cases plotted in Fig. 4(b) are also correlated with the steady behavior of  $\chi_e$  shown in Fig. 3(b). In addition, in the case of  $\Theta=0.2000$ , we see the strong generation of the zonal flow which is responsible for the significant transport reduction at the saturation of the instability growth. The secondary growth of the zonal flow depending on  $\Theta$  will be discussed in detail in Sec. IV by means of the modulational instability analysis with a truncated fluid model.

The power spectra of potential and temperature fluctuations in the cases of  $\Theta=\{0.050, 0.150, 0.200\}$  are shown in Figs. 5(a)–5(c), respectively, where the quantities are summed over  $k_x$ -components and are time-averaged in the early and the late nonlinear phases. Here, the temperature fluctuation is defined by  $\delta T_{k_\perp} \equiv \int d v_{\parallel} (v_{\parallel}^2 - 1) \delta f_{k_\perp}$ . The case of  $\Theta=0.050$  [Fig. 5(a)] shows the significant reduction of higher wave number components of  $|\delta\psi_{k_y}|$  and  $|\delta T_{k_y}|$  in the late nonlinear phase in comparison with those in the early phase. Thus, the transitional behavior is expected to appear not only for the heat diffusivity, but also for potential and temperature fluctuation profiles in the real space.<sup>23</sup> On the other hand, no significant change in the spectrum is observed for the two phases in the case of  $\Theta=0.150$  [Fig. 5(b)]. This is consistent with the steady behavior of the heat diffusivity as shown in Fig. 3(b). The case of  $\Theta=0.200$  [Fig. 5(c)] also shows similar spectrum, while the amplitudes of  $|\delta T_{k_y}|$  and  $|\delta\psi_{k_y}|$  are smaller than those in the case of  $\Theta=0.150$ . This implies that the strong zonal flow generation in the case of  $\Theta=0.200$  [see Fig. 4(b)] suppresses the development of turbulent fluctuations.

Color contours of potential and temperature fluctuations in the real space at  $t=3480$  are shown in Figs. 6(a)–6(e) and

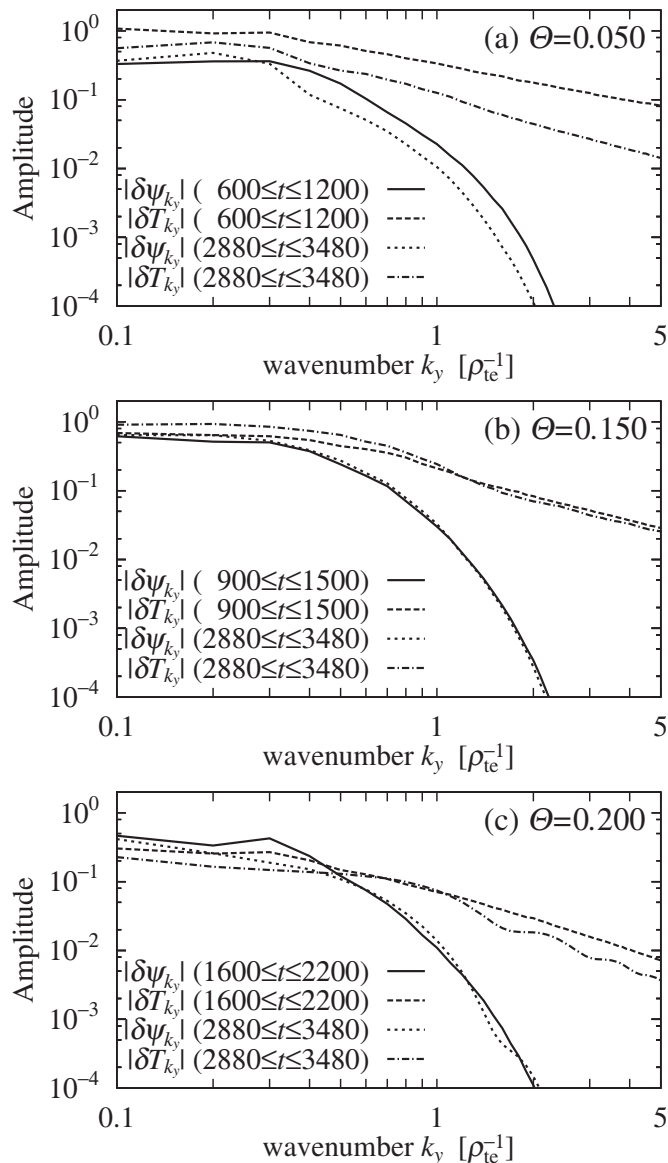


FIG. 5. Time-averaged power spectra of  $|\delta\psi_{k_\perp}|$  and  $|\delta T_{k_\perp}|$  for (a)  $\Theta=0.050$ , (b)  $\Theta=0.150$ , and (c)  $\Theta=0.200$ , where the quantities are summed over  $k_x$ . Each line in the figures shows the results with different time intervals. The units of  $|\delta\psi_{k_y}|$  and  $|\delta T_{k_y}|$  are  $T_e \rho_{te} / e L_T$  and  $T_e \rho_{te} / L_T$ , respectively.

Figs. 6(f)–6(j), respectively. Depending on  $\Theta$ , three different types of vortex structures are clearly observed in the late nonlinear phase, i.e., coherent vortex streets [Figs. 6(a), 6(b), 6(f), and 6(g)], turbulent vortices [Figs. 6(c), 6(d), 6(h), and 6(i)], and zonal-flow-dominated states [Figs. 6(e) and 6(j)]. It should be noted here that the coherent vortex streets, which appear in the cases of smaller value of  $\Theta \leq 0.1$ , are formed by the transition from turbulent vortices found in the early nonlinear phase, while no transition is observed for the other cases. The formation of the coherent vortex streets is associated with the phase matching of  $\delta\phi$  and  $\delta T$ , where the heat transport is significantly reduced. On the other hand, for the cases of the turbulent vortices with  $\Theta=\{0.133, 0.150\}$ , the temperature fluctuations involve much finer scale structures than those in the potential fluctuations. We have verified that the transition of vortex structures, which depends on  $\Theta$ , is commonly observed for the other cases with  $\eta_e=\{7, 8, 9\}$ .

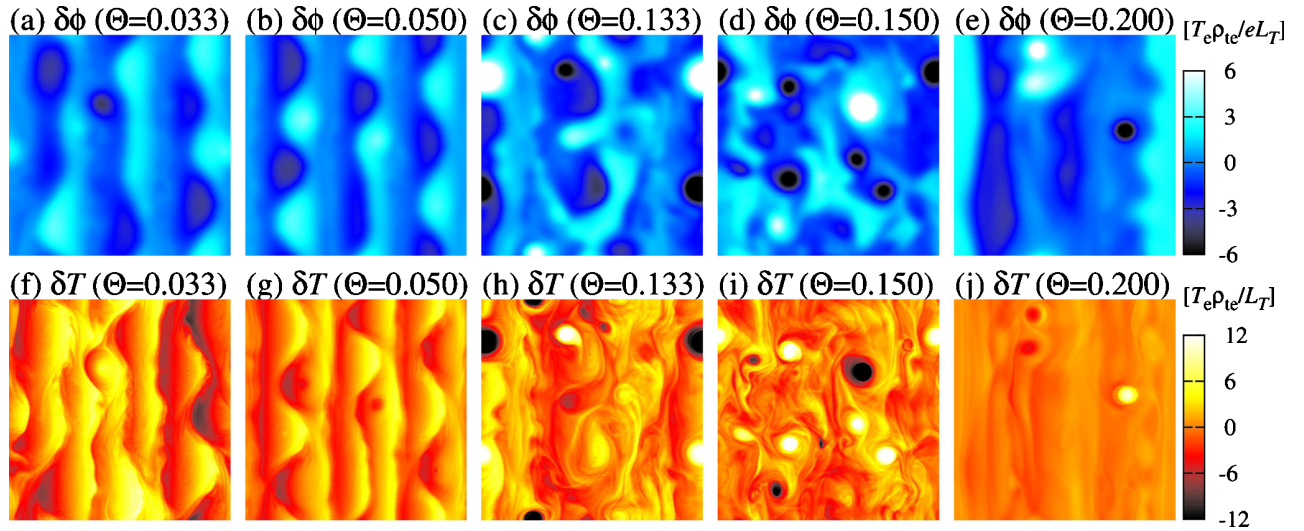


FIG. 6. (Color online) Contours of [(a)–(e)] potential and [(f)–(j)] temperature fluctuations for  $\Theta = \{0.033, 0.050, 0.133, 0.150, 0.200\}$  at  $t = 3480$ , where the box size is  $20\pi\rho_{te} \times 20\pi\rho_{te}$ .

Let us consider a quantity that represents the effect of the parallel compression on the formation of coherent vortex structures. From the Eqs. (1) and (3), one can derive the fluid equation for  $\delta\psi_{k_\perp}$  as follows:

$$\begin{aligned} \frac{\partial}{\partial t} \Lambda_{k_\perp} \delta\psi_{k_\perp} - i\Theta k_y \delta u_{k_\perp} - ik_y \left( \frac{1}{\eta_e} - \frac{k_\perp^2}{2} \right) \delta\psi_{k_\perp} \\ - \sum_{\Delta} \mathbf{b} \cdot (\mathbf{k}'_\perp \times \mathbf{k}''_\perp) \delta\psi_{k'_\perp} \Lambda_{k''_\perp} \delta\psi_{k''_\perp} = 0, \end{aligned} \quad (6)$$

where the normalized quantities are used. The parallel flow is defined by  $\delta u_{k_\perp} \equiv \int d v_{\parallel} v_{\parallel} \delta f_{k_\perp}$ . Equation (6) is reduced to the Hasegawa–Mima-like equation (designated as HM- $\eta_e$  equation in Ref. 23) in the limit of  $\Theta \rightarrow 0$  and the long-wavelength approximation, where the terms up to  $\mathcal{O}(k_\perp^2)$  are kept. Here, we define a quantity representing a relative magnitude of the parallel compression term (the second term) to the diamagnetic drift term (the third term) in Eq. (6), i.e.,  $\mathcal{R} \equiv \eta_e \Theta \Sigma_{k_\perp} \text{Re}[\delta u_{k_\perp} \delta \psi_{k_\perp}^*] / \Sigma_{k_\perp} |\delta \psi_{k_\perp}|^2$ . From the turbulence simulation results, it is found that  $\bar{\mathcal{R}} \approx 0.33$  for  $\Theta = 0.050$ ,  $\bar{\mathcal{R}} \approx 0.87$  for  $\Theta = 0.150$ , and  $\bar{\mathcal{R}} \approx 1.41$  for  $\Theta = 0.200$ , where the time average is taken for  $2500 \leq t \leq 3500$ . The small value of  $\bar{\mathcal{R}}$  for  $\Theta = 0.050$  suggests that the coherent vortex streets are approximately described by a traveling wave solution of the HM- $\eta_e$  equation derived from Eq. (6) in the limit of  $\Theta \rightarrow 0$  (see Ref. 23). In contrast, for the cases with relatively larger  $\Theta$  or  $\bar{\mathcal{R}}$ , the Hasegawa–Mima model is no longer valid. Thus, the effect of the finite parallel compression, which causes couplings with the higher-order fluid moments through electrostatic acoustic modes for electrons, becomes more important.

## B. Summary of parameter studies

Let us briefly summarize the vortex structures associated with zonal flows and the related transport properties found in the present parameter study of the slab ETG turbulence. The results of the  $\Theta$ -dependence of time-averaged values of the

normalized zonal flow energy  $W_{zf}/W$  are shown in Fig. 7, where all cases of  $\eta_e$  are plotted. For reference, we also plotted the corresponding maximum growth rates of the linear ETG modes  $\gamma_{L(\max)}$  in the figure. One clearly finds that the strong zonal flow is generated in the regions of  $\Theta \leq 0.1$  and  $\Theta \geq 1.8$ , corresponding to the formation of coherent vortex streets and the zonal-flow-dominated structure, respectively. The zonal flow generation is weaker in the region of  $0.1 \leq \Theta \leq 1.8$ , where the turbulent vortices are observed. It is also remarkable that the similar  $\Theta$ -dependence of  $W_{zf}/W$  is found in all cases of  $\eta_e = \{6, 7, 8, 9\}$ . This implies that the transition of the vortex structures in the slab ETG turbulence is mainly controlled by  $\Theta$  rather than  $\eta_e$  if the value of  $\eta_e$  is large enough. Actually, in all cases of  $\eta_e$ , the completely different vortex structures have been realized depending on  $\Theta$ , even for the cases with the same maximum growth rate  $\gamma_{L(\max)}$ . It is confirmed by the fact that for  $\eta_e = 6$ , the cases of  $\Theta = \{0.033, 0.133\}$  with the same  $\gamma_{L(\max)}$  show quite different levels of  $W_{zf}/W$ .

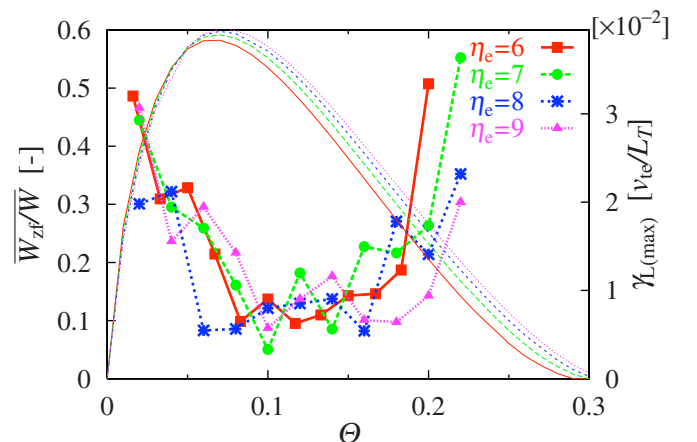


FIG. 7. (Color online) Time-averaged value of  $W_{zf}/W$  as a function of  $\Theta$  for  $\eta_e = \{6, 7, 8, 9\}$ , where the time average is taken for the late nonlinear phase ( $2500 \leq t \leq 3500$ ). Maximum linear growth rates are also shown by solid lines with the same colors.

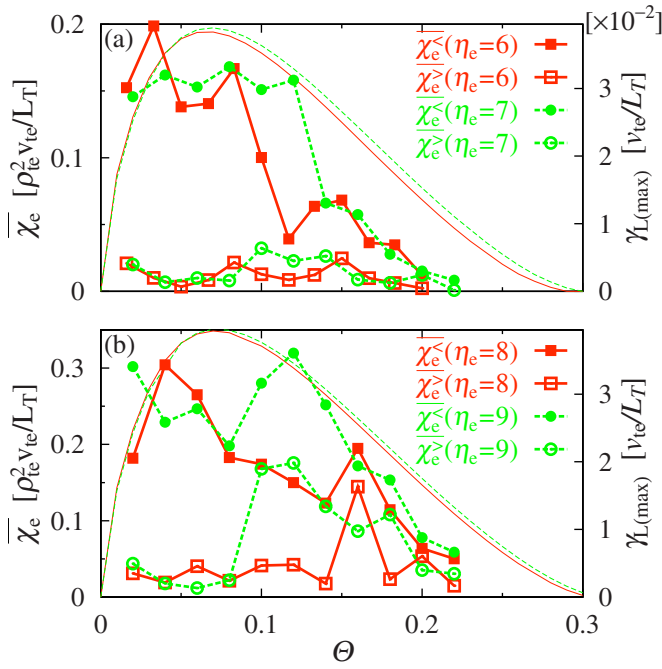


FIG. 8. (Color online) Time-averaged value of  $\chi_e$  as a function of  $\Theta$  for (a)  $\eta_e=\{6,7\}$  and (b)  $\eta_e=\{8,9\}$ , where  $\chi_e^<$  and  $\chi_e^>$  represent the values averaged over the early and late nonlinear phases, respectively. Maximum linear growth rates are also shown by solid lines with the same colors.

In order to discuss the relation between the transition of vortex structures and the transport reduction, we plotted in Figs. 8(a) and 8(b) the  $\Theta$ -dependence of  $\chi_e$  averaged over the early and late nonlinear phases for  $\eta_e=\{6,7\}$  and  $\eta_e=\{8,9\}$ , respectively. One finds that the distinct difference between  $\chi_e^<$  and  $\chi_e^>$  indicating the transport reduction is commonly found in the region of  $\Theta \lesssim 0.1$  for all values of  $\eta_e$ . Also, we see the qualitatively similar dependence of  $\chi_e$  on  $\Theta$  such that the reduction of  $\chi_e$  becomes smaller for the larger  $\Theta$ . It is remarkable that for small  $\Theta$ , the transport reduction associated with the formation of coherent vortex streets is realized in the nonlinear phase, even if the maximum growth rate of linear ETG modes is relatively large.

#### IV. MODULATIONAL INSTABILITY ANALYSIS FOR ZONAL FLOW GENERATION

In Sec. III, it is found that the formation of coherent vortex structures is closely related to the secondary growth of zonal flows in the nonlinear phase as shown in Fig. 4. Here, we discuss the dependence of zonal flow generation on  $\Theta(=k_{\parallel}L_T/k_y\rho_{te})$  based on the modulational instability analysis with a truncated fluid model, where the parallel dynamics such as electron acoustic modes due to the parallel compression is taken into account. These analyses give us qualitative understanding for mechanisms of the secondary growth of zonal flows found in the ETG turbulence simulations.

Here, we consider truncated fluid equations for the modulational instability analysis. In the derivation of the fluid model below, we employ the description with dimensional quantities again. By taking the fluid moments of the gyrokinetic equation [see Eq. (1)] up to the second order, one obtains the following equations:

$$\begin{aligned} \frac{\partial}{\partial t} \delta n_{k_{\perp}} + ik_{\parallel} n_0 \delta u_{k_{\perp}} + i\omega_{*e} n_0 \left(1 - \frac{\eta_e k_{\perp}^2 \rho_{te}^2}{2}\right) \frac{e \delta \psi_{k_{\perp}}}{T_e} \\ - \frac{c}{B} \sum_{\Delta} \mathbf{b} \cdot (\mathbf{k}'_{\perp} \times \mathbf{k}''_{\perp}) \delta \psi_{k'_{\perp}} \delta n_{k''_{\perp}} = 0, \end{aligned} \quad (7)$$

$$\begin{aligned} n_0 m_e \frac{\partial}{\partial t} \delta u_{k_{\perp}} + ik_{\parallel} (T_e \delta n_{k_{\perp}} + n_0 \delta T_{k_{\perp}} - n_0 e \delta \psi_{k_{\perp}}) \\ - \frac{n_0 m_e c}{B} \sum_{\Delta} \mathbf{b} \cdot (\mathbf{k}'_{\perp} \times \mathbf{k}''_{\perp}) \delta \psi_{k'_{\perp}} \delta u_{k''_{\perp}} = 0, \end{aligned} \quad (8)$$

$$\begin{aligned} n_0 \frac{\partial}{\partial t} \delta T_{k_{\perp}} + ik_{\parallel} (2n_0 T_e \delta u_{k_{\perp}} + \delta q_{k_{\perp}}) + i\omega_{*e} \eta_e n_0 e \delta \psi_{k_{\perp}} \\ - \frac{n_0 c}{B} \sum_{\Delta} \mathbf{b} \cdot (\mathbf{k}'_{\perp} \times \mathbf{k}''_{\perp}) \delta \psi_{k'_{\perp}} \delta T_{k''_{\perp}} = 0, \end{aligned} \quad (9)$$

where the fluid quantities are defined by  $\delta n_{k_{\perp}} \equiv \int d v_{\parallel} \delta f_{k_{\perp}}$ ,  $n_0 \delta u_{k_{\perp}} \equiv \int d v_{\parallel} v_{\parallel} \delta f_{k_{\perp}}$ ,  $n_0 \delta T_{k_{\perp}} \equiv \int d v_{\parallel} (m_e v_{\parallel}^2 - T_e) \delta f_{k_{\perp}}$ , and  $\delta q_{k_{\perp}} \equiv \int d v_{\parallel} (m_e v_{\parallel}^3 - 3T_e v_{\parallel}) \delta f_{k_{\perp}}$ , which denote the fluctuations of the density, the parallel flow, the temperature, and the parallel heat flux, respectively. Here, the collisional dissipation is neglected because of  $\nu_e L_T / v_{te} \ll 1$ .

In order to derive a reduced model describing the evolution of zonal flows, we postulate here that (i) the fluid equations are truncated by ignoring the parallel heat flux  $\delta q_{k_{\perp}}$  in Eq. (9) and that (ii) the third term  $i\omega_{*e} \eta_e n_0 e \delta \psi_{k_{\perp}}$ , which drives the linear ETG instability, is also neglected in Eq. (9). The first assumption (i) is necessary for the truncation of the couplings of fluid equations. The second one (ii) is useful for the analysis of modulational instabilities driven by the “stable” pump wave because we focus on the secondary growth of zonal flows after the initial saturation, where the ETG mode no longer grows linearly. Furthermore, (iii) we neglect the nonlinear terms in Eqs. (8) and (9) for simplicity because they cause higher-order interactions which are not of interest here. Under these assumptions, the reduced fluid equations used here are derived by means of the quasineutrality condition Eq. (3)

$$\left(\frac{\partial}{\partial t} - i\mathcal{L}_{k_{\perp}}\right) \psi_{k_{\perp}} - ik_{\parallel} v_{te} \Lambda_{k_{\perp}}^{-1} u_{k_{\perp}} - \sum_{\Delta} \Gamma_{k_{\perp}}^{k'_{\perp}, k''_{\perp}} \psi_{k'_{\perp}} \psi_{k''_{\perp}} = 0, \quad (10)$$

$$\frac{\partial}{\partial t} u_{k_{\perp}} + ik_{\parallel} v_{te} [T_{k_{\perp}} - (1 + \Lambda_{k_{\perp}}) \psi_{k_{\perp}}] = 0, \quad (11)$$

$$\frac{\partial}{\partial t} T_{k_{\perp}} + 2ik_{\parallel} v_{te} u_{k_{\perp}} = 0, \quad (12)$$

where

$$\mathcal{L}_{k_{\perp}} \equiv \omega_{*e} \left(1 - \frac{\eta_e k_{\perp}^2 \rho_{te}^2}{2}\right) \Lambda_{k_{\perp}}^{-1}, \quad (13)$$

$$\Gamma_{k_{\perp}^{\prime}, k_{\perp}^{\prime\prime}} \equiv \frac{1}{2} \frac{cT_e}{eB} \mathbf{b} \cdot (\mathbf{k}_{\perp}^{\prime} \times \mathbf{k}_{\perp}^{\prime\prime}) (\Lambda_{k_{\perp}^{\prime\prime}} - \Lambda_{k_{\perp}^{\prime}}) \Lambda_{k_{\perp}^{\prime}}^{-1}. \quad (14)$$

Here, abbreviations for  $\psi_{k_{\perp}} \equiv e \delta \psi_{k_{\perp}} / T_e$ ,  $u_{k_{\perp}} \equiv \delta u_{k_{\perp}} / u_{te}$ , and  $T_{k_{\perp}} \equiv \delta T_{k_{\perp}} / T_e$  are used. The symbol  $\sum_{\Delta}$  means the summation over the Fourier modes which consist of the triad interaction, i.e.,  $\mathbf{k}_{\perp} = \mathbf{k}_{\perp}^{\prime} + \mathbf{k}_{\perp}^{\prime\prime}$ . The above reduced fluid equations involve the effect of electron acoustic modes due to the parallel compression which has rarely been incorporated into the conventional modulational instability analysis for the zonal flow generation.<sup>19,24–27</sup>

In order to derive the dispersion equation for zonal flows driven by the modulational instability, we consider the low-dimensional model (sometimes called the four-wave model) based on Eqs. (10)–(14). The field quantities  $\xi = \{\psi, u, T\}$  are then assumed to be composed of a monochromatic pump mode, a zonal mode, and two sideband modes, such that

$$\begin{aligned} \xi(\mathbf{x}, t) = & \xi_{k_p} \exp(i\mathbf{k}_p \cdot \mathbf{x} - i\omega_{k_p} t) + \xi_{k_{zf}} \exp(i\mathbf{k}_{zf} \cdot \mathbf{x} - i\Omega_{k_{zf}} t) \\ & + \xi_{k^+} \exp(i\mathbf{k}^+ \cdot \mathbf{x} - i\omega_{k^+} t) \\ & + \xi_{k^-} \exp(i\mathbf{k}^- \cdot \mathbf{x} - i\omega_{k^-} t) \\ & + (\text{complex conjugate}), \end{aligned} \quad (15)$$

where the complex frequency and the wave number vector of these four modes satisfy the frequency matching and the triad-interaction conditions, respectively, as follows:

$$\omega_{k^{\pm}} = \omega_{k_p} \pm \Omega_{k_{zf}}, \quad \mathbf{k}^{\pm} = \mathbf{k}_p \pm \mathbf{k}_{zf}. \quad (16)$$

Also,  $k_{\parallel p} = k_{\parallel}^{\pm}$  ( $\equiv k_{\parallel}$ ) and  $\xi_k = \xi_{k^*}$ . The reduction to four resonant modes from Eqs. (10)–(14) leads to a nonlinear dynamical system of four ordinary differential equations. Here, we suppose that the complex amplitude of the zonal and the sideband modes are much smaller than that of the pump mode, i.e.,

$$|\xi_{k_{zf}}| \sim |\xi_{k^{\pm}}| \sim \epsilon |\xi_{k_p}|, \quad (17)$$

where  $\epsilon \ll 1$ . This subsidiary ordering enables us to linearize the nonlinear system so that one obtains the dispersion relation which determines the linear growth rate of zonal flows.

For the pump mode, one obtains the following equations:

$$\begin{aligned} i(\omega_{k_p} + \mathcal{L}_{k_p}) \psi_{k_p} + ik_{\parallel} u_{te} \Lambda_{k_p}^{-1} u_{k_p} + \Gamma_{k_p}^{k^-, k_{zf}} \psi_{k^-} \psi_{k_{zf}} \\ + \Gamma_{k_p}^{k^+, -k_{zf}} \psi_{k^+} \psi_{k_{zf}}^* = 0, \end{aligned} \quad (18)$$

$$i\omega_{k_p} u_{k_p} - ik_{\parallel} u_{te} [T_{k_p} - (1 + \Lambda_{k_p}) \psi_{k_p}] = 0, \quad (19)$$

$$i\omega_{k_p} T_{k_p} - 2ik_{\parallel} u_{te} u_{k_p} = 0. \quad (20)$$

Considering the ordering of Eq. (17), one can neglect the last two terms on the left hand side of Eq. (18), which are of order  $\epsilon^2 |\psi_{k_p}|^2$ , so that Eqs. (18)–(20) are reduced to the dispersion equation for the pump mode as follows:

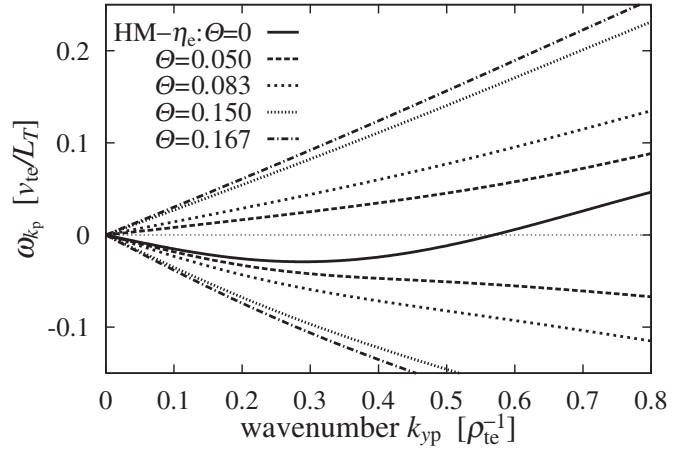


FIG. 9. Real frequency of the pump mode  $\omega_{k_p}$  for  $\Theta = \{0, 0.050, 0.083, 0.150, 0.167\}$ , where  $\eta_e = 6$  and  $k_{xp} = 0.1$ .

$$1 + \frac{\mathcal{L}_{k_p}}{\omega_{k_p}} - \left( \frac{1 + \Lambda_{k_p}}{\Lambda_{k_p}} \right) \left( \frac{k_{\parallel} u_{te}}{\omega_{k_p}} \right)^2 \left[ 1 - 2 \left( \frac{k_{\parallel} u_{te}}{\omega_{k_p}} \right)^2 \right]^{-1} = 0. \quad (21)$$

This can be rewritten as a cubic equation of  $\omega_{k_p}$  and then the root determines the frequency of the pump mode for given  $\mathbf{k}_p$  and  $k_{\parallel}$ . By evaluating the sign of the discriminant of Eq. (21), it is easily shown that any root must be real-valued. Thus, there is neither instability nor damping. The dispersion relation of  $\omega_{k_p}$  for  $\Theta = \{0, 0.050, 0.083, 0.150, 0.167\}$  are shown in Fig. 9, where  $\eta_e = 6$  and  $k_{xp} = 0.1$ . For the case of  $\Theta \neq 0$ , we plotted two of the three branches (the branches with positive and negative  $\omega_{k_p}$ ), which approach the solution of HM- $\eta_e$  equation in the limit of  $\Theta \rightarrow 0$  ( $k_{\parallel} \rightarrow 0$ ). Another branch, which is not plotted here, approaches to the trivial solution of  $\omega_{k_p} = 0$ . As expected, we see that the deviation of the frequency from that for  $\Theta = 0$  becomes larger as  $\Theta$  increases.

From Eqs. (10)–(17), one obtains the equations for zonal and sideband modes as follows:

$$i\Omega_{k_{zf}} \psi_{k_{zf}} + \Gamma_{k_{zf}}^{k^+, -k_p} \psi_{k^+} \psi_{k_p}^* + \Gamma_{k_{zf}}^{k^-, k_p} \psi_{k^-} \psi_{k_p} = 0, \quad (22)$$

$$i\mathcal{P}_{\pm} \psi_{k^{\pm}} + \Gamma_{k^{\pm}}^{k_p, \pm k_{zf}} \psi_{k_p} \psi_{\pm k_{zf}} = 0, \quad (23)$$

where

$$\mathcal{P}_{\pm} \equiv \omega_{k^{\pm}} [1 + \mathcal{K}_{k^{\pm}}(\omega_{k^{\pm}}, k_{\parallel})] + \mathcal{L}_{k^{\pm}}. \quad (24)$$

Here, the effect of the coupling among  $\psi_{k^{\pm}}$ ,  $u_{k^{\pm}}$  and  $T_{k^{\pm}}$  for sideband modes due to the parallel compression appears in  $\mathcal{K}_{k^{\pm}}(\omega_{k^{\pm}}, k_{\parallel})$  defined as

$$\mathcal{K}_{k^{\pm}}(\omega_{k^{\pm}}, k_{\parallel}) \equiv - \left( \frac{1 + \Lambda_{k^{\pm}}}{\Lambda_{k^{\pm}}} \right) \left( \frac{k_{\parallel} u_{te}}{\omega_{k^{\pm}}} \right)^2 \left[ 1 - 2 \left( \frac{k_{\parallel} u_{te}}{\omega_{k^{\pm}}} \right)^2 \right]^{-1}. \quad (25)$$

These terms, which are ignored in the conventional analysis with the Hasegawa–Mima equation, play a crucial role in considering the effect of the finite parallel compression on the zonal flow generation. Indeed, one can obtain the con-

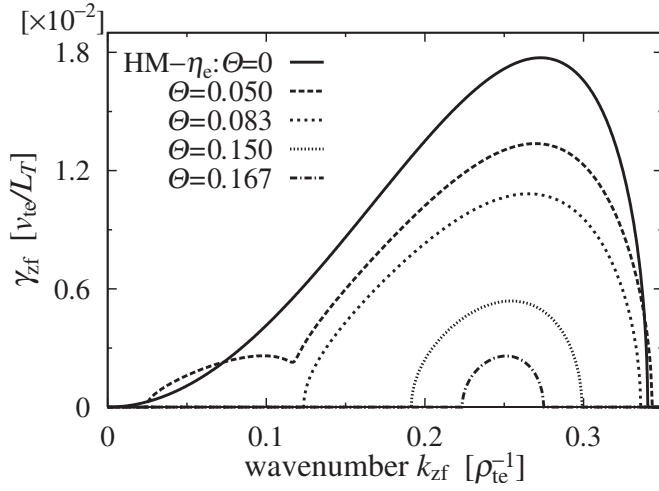


FIG. 10. Growth rate of zonal flows  $\gamma_{zf}$  for  $\Theta=\{0, 0.050, 0.083, 0.150, 0.167\}$ , where  $k_{xp}=0.1$ ,  $k_{yp}=0.35$ , and  $(L_T/\rho_{te})^2|\psi_{kp}|^2=2$ .

ventional dispersion relation in the limit of  $k_{\parallel} \rightarrow 0$  which annihilates  $\mathcal{K}_{k^{\pm}}$  in Eq. (24), as well as in the long-wavelength limit ( $k_{\perp}\rho_{te} \ll 1$ ). Finally, combining Eqs. (21)–(25), one obtains the dispersion relation of zonal flows as follows:

$$\Omega_{k_{zf}} + \left[ \frac{\Gamma_{k_{zf}}^{k^+, -k_p} \Gamma_{k_{zf}}^{k_{zf}, k_p}}{\mathcal{P}_+} - \frac{\Gamma_{k_{zf}}^{k^-, -k_p} \Gamma_{k_{zf}}^{-k_{zf}, k_p}}{\mathcal{P}_-} \right] |\psi_{k_p}|^2 = 0. \quad (26)$$

The linear growth rate of zonal flows  $\gamma_{zf}$  is then given by the positive imaginary part of a complex solution  $\Omega_{k_{zf}}$  of the above equation. Straightforward but somewhat tedious algebraic calculation shows that the left hand side of Eq. (26) is rearranged into a seventh-order polynomial of  $\Omega_{k_{zf}}$  with real-valued coefficients, which has to be solved numerically. In the numerical calculations, we have found only two cases, namely, solutions with a pair of complex conjugate and five real-valued roots or with seven real-valued roots.

Figure 10 shows the spectrum of the zonal flow growth rate  $\gamma_{zf}$  for  $\Theta=\{0, 0.050, 0.083, 0.150, 0.167\}$ , where the wave number and the amplitude of the pump mode are chosen as  $k_{xp}=0.1$ ,  $k_{yp}=0.35$ , and  $(L_T/\rho_{te})^2|\psi_{kp}|^2=2$ , respectively. Here, the branch of the negative  $\omega_{k_p}$  (see Fig. 9) are chosen because, for  $k_{yp}=0.35$ , it converges to the nontrivial dispersion relation ( $\omega_{k_p} \neq 0$ ) in the limit of  $\Theta \rightarrow 0$ . One clearly finds that growth rate of the modulational instability for zonal flows is decreased by increasing  $\Theta$  and no unstable solution exists for  $\Theta \geq 0.167$ .

In order to discuss  $\Theta$ -dependence of the critical pump amplitude for the instability onset, we plotted in Fig. 11 the maximum growth rate of the zonal flow  $\gamma_{zf(\max)}$  as a function of the squared amplitude of the pump mode  $(L_T/\rho_{te})^2|\psi_{kp}|^2$ . From this figure, we find that the critical amplitude for the instability becomes larger as  $\Theta$  increases. In the region where the pump amplitude is sufficiently large [e.g.,  $(L_T/\rho_{te})^2|\psi_{kp}|^2 \geq 3$ ], the instabilities are observed for all cases of  $\Theta$ . However, in the region of  $(L_T/\rho_{te})^2|\psi_{kp}|^2 \leq 2$ , one can see the existence of a critical value of  $\Theta$ , beyond which the

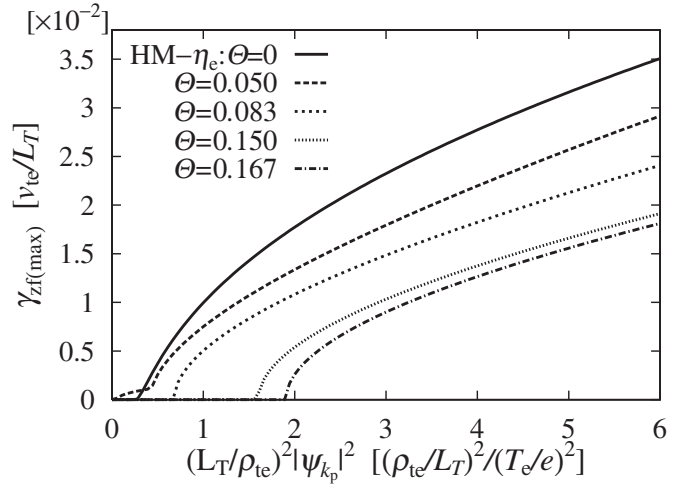


FIG. 11. Maximum growth rate of zonal flows  $\gamma_{zf(\max)}$  as a function of  $(L_T/\rho_{te})^2|\psi_{kp}|^2$  for  $\Theta=\{0, 0.050, 0.083, 0.150, 0.167\}$ . The wave numbers of the pump mode are the same as those in Fig. 10.

instability no longer occurs. In the present ETG turbulence simulations, we find  $(L_T/\rho_{te})^2|\psi_{kp}|^2 \sim 1$ . Hence, the critical  $\Theta$  is estimated as  $\Theta \sim 0.1$ , which qualitatively agrees with that for the secondary growth of zonal flows found in the cases of small  $\Theta$  [see Figs. 4(a) and 4(b)].

We also plot in Fig. 12 the maximum growth rate  $\gamma_{zf(\max)}$  and the real frequency  $\omega_{zf}$  for  $\eta_e=\{6, 7, 8, 9\}$  as a function of  $\Theta$ , where  $\omega_{zf}$  is evaluated at the wave number giving the maximum growth rate. One finds that the maximum growth rate  $\gamma_{zf(\max)}$  shows the similar dependence on  $\Theta$  for all values of  $\eta_e$  considered, except that the profiles are shifted downward. The stable region of  $\Theta$  with  $\gamma_{zf(\max)}=0$  then becomes

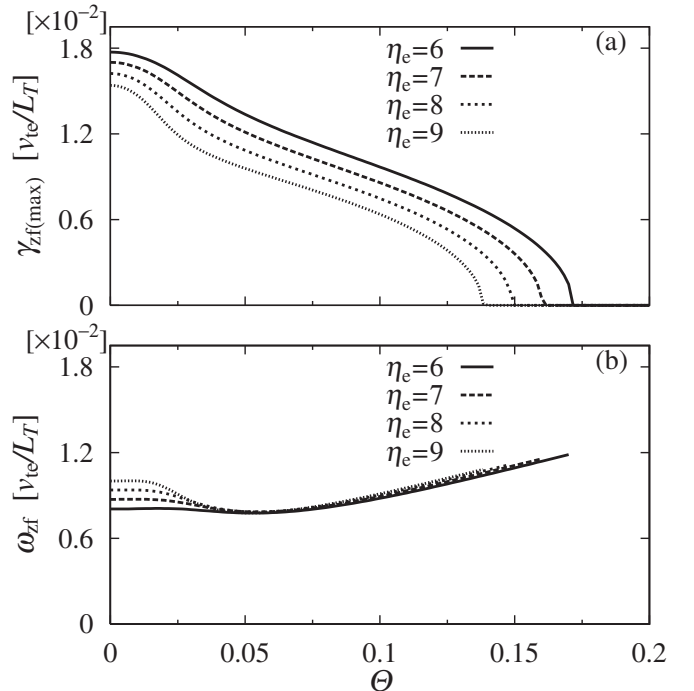


FIG. 12. (a) Maximum growth rate  $\gamma_{zf(\max)}$  and (b) real frequency  $\omega_{zf}$  for zonal flows as a function of  $\Theta$  for  $\eta_e=\{6, 7, 8, 9\}$ . The wave numbers and the amplitude of the pump mode are the same as those in Fig. 10.

wider for larger  $\eta_e$ . Also, we see that the value of  $\omega_{zf}$  is larger than that of  $\gamma_{zf(\max)}$  in the region of  $\Theta \gtrsim 0.1$ , which means the oscillatory zonal flow. Since the steady zonal flow suppresses the turbulent transport more effectively compared to the oscillatory one, these results suggest that the relatively steady zonal flow with larger growth rate can be driven for smaller  $\eta_e$  if the pump amplitude is fixed. However, the pump amplitude is, in practice, associated with the turbulence intensity which should depend on  $\eta_e$ . Nevertheless, it is important that the critical value of  $\Theta$ , which define the instability onset, commonly appears for all cases of  $\eta_e$  and then these results well explain the turbulence simulation results.

Here, we have derived the dispersion relation of zonal flows based on the modulational instability analysis, where the coupling of fluid moments (density, parallel flow, and temperature) through the parallel compression term is incorporated. The results then show the stabilizing effect due to the parallel compression which is proportional to  $\Theta$ .

The present theoretical analysis with a stable pump mode provides us with the qualitative explanations of the turbulence simulation results for  $0 \leq \Theta \leq 0.15$ . However, the analysis is limited to the case where the nonzonal fluctuations are dominant in the saturated ETG turbulence because the subsidiary ordering Eq. (17) for the modulational instability analysis assumes the quite low amplitude of the zonal mode in comparison with the pump amplitude. It is, thus, not directly applicable to the case with the generation of the strong zonal flow accompanied with the transport suppression observed in the turbulence simulation for  $\Theta \geq 0.200$  [see Figs. 4(b) and 7], where the strong zonal flow is predominantly generated by the nonlinear coupling of linear ETG modes in the initial saturation phase of the instability growth [e.g.,  $t \approx 1200$  for  $\Theta = 0.200$  in Fig. 4(b)]. In order to reveal the detailed mechanisms of the initial generation of strong zonal flows with the effect of parallel compression, one needs more refinement of the present model to incorporate the unstable evolution of the pump mode precisely, which remains as a future work.

The coupling among the fluid moments of  $\{\psi, u, T\}$  considered here suggests the importance of the parallel dynamics on the stability of zonal flows. It has also been verified that the similar stabilization of zonal flows due to the parallel compression is observed in a model with only a coupling of  $\{\psi, u\}$ . Anderson *et al.*<sup>29</sup> had previously derived the dispersion relation of zonal flows for ITG turbulence by the similar approach with the fluid equations and then they showed fifth-order polynomial of  $\Omega_{k_{zf}}$  which differs from our dispersion equation of seventh-order polynomial as shown in Eq. (26). Consequently, the different dependence of  $\gamma_{zf}$  on  $k_{\parallel}$  (or  $\Theta$ ) appears, e.g., the stabilization of zonal flows found in the present analysis for larger  $k_{\parallel}$  is not observed in Ref. 29. This is because the coupling with the parallel flow, which corresponds to the second term of Eq. (12), had been ignored from the temperature equation shown in Ref. 29. Neglecting this term reduces the order of polynomial for the dispersion relation, but leads to an incomplete description of acoustic modes at the same time. The similar modulational instability

analysis for zonal flows/fields involving the parallel dynamics of shear-Alfvén waves had also been examined by Guzdar *et al.*<sup>30</sup> and by Chen *et al.*<sup>31</sup> for the drift-Alfvén turbulence.

## V. CONCLUDING REMARKS

We have investigated the transition of vortex structures including zonal flows and the related transport properties in the slab ETG turbulence through the comprehensive parameter studies by means of the nonlinear gyrokinetic Vlasov simulations. Then, the dependence on the magnitude of the parallel compression, which is characterized by the parameter  $\Theta \equiv k_{\parallel} L_T / k_y \rho_{te} = \theta L_T / \rho_{te}$ , and the electron temperature gradient have been intensively examined.

Numerical results show three different types of the time evolution of the heat diffusivity depending on  $\Theta$ , i.e., transitional evolution accompanied with transport reduction, steady turbulent behavior, and significant suppression of transport. Then, the zonal flow evolutions with or without secondary growth in the nonlinear phase are well correlated with the evolution of the heat diffusivity. Correspondingly, the detailed analyses of the spectral and the spatial structures of the potential and temperature fluctuations reveal the different types of vortex structures such as coherent vortex streets, turbulent vortices, and zonal-flow-dominated state. The vortex structures depend on the value of  $\Theta$  through the parallel compression.

By examining the dependence of the heat diffusivity and the intensity of zonal flows on  $\Theta$ , we found clear correlation between the formation of coherent vortex streets associated with the strong generation of the zonal flow and transport reduction for the cases with small values of  $\Theta \lesssim 0.1$ . These results indicate weak dependence on the value of  $\eta_e$ , which implies that the transition of vortex structures in the slab ETG turbulence is mainly controlled by  $\Theta$  rather than  $\eta_e$  if  $\eta_e$  is large enough. The transport reduction associated with the formation of coherent vortex streets is realized for small  $\Theta$  even if the maximum growth rate of linear ETG modes is relatively large.

We have discussed the dependence of zonal flow generation on  $\Theta$  based on the modulational instability analysis with a truncated fluid model, where the parallel dynamics associated with electron acoustic modes is taken into account. The dispersion relation of zonal flows derived here shows that the linear growth rate of the modulational instability is reduced as  $\Theta$  increases and that there is a critical value of  $\Theta$ , beyond which the instability does not occur. The modulational instability analysis shows a qualitative agreement with the turbulence simulation results, where the secondary growth of zonal flows, the transition of vortex structures, and the related transport reduction are found in the cases of small  $\Theta$ .

In the present study, the quasi-two-dimensional shearless slab configuration has been employed, where  $\Theta$  and  $\eta_e$  are the main control parameters. Although the various values of  $\Theta$  should be treated simultaneously in cylindrical or toroidal plasmas, the two-dimensional slab configuration with constant  $\Theta$  used here is still meaningful as a reduced model for them. In these practical systems,  $k_{\parallel}/k_y$  depends on the aspect

ratio  $L_z/a$  (“the length of plasma column”/“the plasma radius”) for cylindrical plasmas or depends on the radial position through the magnetic shear for toroidal ones. Particularly, in the toroidal plasmas, it has been pointed out that the compression due to the geodesic curvature and the toroidal mode coupling become more important for the saturation of the toroidal ETG instability with strong magnetic shear, where the toroidal modes overlap each other significantly.<sup>14,15</sup> However, in the case with weak magnetic shear, the unstable-mode rational surfaces become more distant from each other so that the toroidal mode coupling weakens. The present study on the slab ETG turbulence may contribute to fundamental understandings of the effects of the parallel compression on the long-timescale evolution of zonal flows and the related transport reduction on the neighborhood of the minimum- $q$  surface ( $q$  denotes the safety factor) in the reversed-shear tokamaks.

In Refs. 14 and 15, it has also been pointed out that the three-wave resonant interaction is crucial for the saturation of the toroidal ETG instability, rather than the zonal flow generation due to the modulational instability. Here, we have not quantitatively examined which of the three-wave interaction and the zonal flow generation driven by the modulational instability is dominant in the initial saturation of the slab ETG instability. Nevertheless, it is expected that the initial saturation is attributed to not only the three-wave interaction, but also to the zonal flow generation because the zonal flow generation in the slab ETG turbulence is stronger than that in the toroidal ETG case where the zonal flow is weakened by the neoclassical polarization effect. It should be emphasized here that the present study reveals the importance of the long-timescale evolution of zonal flows, which is closely related to the transition of vortex structures and transport level in the nonlinear phase long after the initial saturation of the slab ETG instability. Then, the long-timescale evolution of zonal flows generated by the modulational instability may also be important in the nonlinear phase of the toroidal ETG turbulence.

The detailed analysis of the initial saturation and the extension to the cylindrical and the toroidal configurations are currently in progress, where the possibility of the formation of coherent vortex structures and the related transport reduction under realistic conditions are investigated as well as the comparison with the experimental observations.

## ACKNOWLEDGMENTS

Numerical computations are performed at the NIFS Plasma Simulator and Supercomputing Resources at Cyber-science Center, Tohoku University. This work is supported in part by the Grant-in-Aid for Japan Society for the Promotion

of Science (Grant No. 20-4017), the Japanese Ministry of Education, Culture, Sports, Science, and Technology Grant No. 21560861, and the NIFS Collaborative Research Programs Grant Nos. NIFS10KTAT040, NIFS10KDAT020, and NIFS10KNXN186.

- <sup>1</sup>W. Horton, *Rev. Mod. Phys.* **71**, 735 (1999).
- <sup>2</sup>A. M. Dimits, G. Bateman, M. A. Beer, B. I. Cohen, W. Dorland, G. W. Hammett, C. Kim, J. E. Kinsey, M. Kotschenreuther, A. H. Kritiz, L. L. Lao, J. Mandrekas, W. M. Nevins, S. E. Parker, A. J. Redd, D. E. Shumaker, R. Sydora, and J. Weiland, *Phys. Plasmas* **7**, 969 (2000).
- <sup>3</sup>B. N. Rogers, W. Dorland, and M. Kotschenreuther, *Phys. Rev. Lett.* **85**, 5336 (2000).
- <sup>4</sup>Z. Lin, T. S. Hahm, W. W. Lee, W. M. Tang, and R. B. White, *Science* **281**, 1835 (1998).
- <sup>5</sup>T.-H. Watanabe, H. Sugama, and S. Ferrando-Margalet, *Phys. Rev. Lett.* **100**, 195002 (2008).
- <sup>6</sup>T.-H. Watanabe and H. Sugama, *Nucl. Fusion* **46**, 24 (2006).
- <sup>7</sup>T.-H. Watanabe and H. Sugama, *Phys. Plasmas* **11**, 1476 (2004).
- <sup>8</sup>H. Sugama, T.-H. Watanabe, and W. Horton, *Phys. Plasmas* **10**, 726 (2003).
- <sup>9</sup>G. W. Hammett and F. W. Perkins, *Phys. Rev. Lett.* **64**, 3019 (1990).
- <sup>10</sup>A. Fujisawa, K. Itoh, H. Iguchi, K. Matsuoka, S. Okamura, A. Shimizu, T. Minami, Y. Yoshimura, K. Nagaoka, C. Takahashi, M. Kojima, H. Nakano, S. Oshima, S. Nishimura, M. Isobe, C. Suzuki, T. Akiyama, K. Ida, K. Toi, S.-I. Itoh, and P. H. Diamond, *Phys. Rev. Lett.* **93**, 165002 (2004).
- <sup>11</sup>F. Jenko, W. Dorland, M. Kotschenreuther, and B. N. Rogers, *Phys. Plasmas* **7**, 1904 (2000).
- <sup>12</sup>W. M. Nevins, J. Candy, S. Cowley, T. Dannert, A. Dimits, W. Dorland, C. Estrada-Mila, G. W. Hammett, F. Jenko, M. J. Pueschel, and D. E. Shumaker, *Phys. Plasmas* **13**, 122306 (2006).
- <sup>13</sup>Z. Lin, I. Holod, L. Chen, P. H. Diamond, T. S. Hahm, and S. Ethier, *Phys. Rev. Lett.* **99**, 265003 (2007).
- <sup>14</sup>Z. Lin, L. Chen, and F. Zonca, *Phys. Plasmas* **12**, 056125 (2005).
- <sup>15</sup>L. Chen, F. Zonca, and Z. Lin, *Plasma Phys. Controlled Fusion* **47**, B71 (2005).
- <sup>16</sup>Y. Idomura, S. Tokuda, and Y. Kishimoto, *Nucl. Fusion* **45**, 1571 (2005).
- <sup>17</sup>Y. Idomura, M. Wakatani, and S. Tokuda, *Phys. Plasmas* **7**, 3551 (2000).
- <sup>18</sup>J. Li, Y. Kishimoto, N. Miyato, T. Matsumoto, and J. Q. Dong, *Nucl. Fusion* **45**, 1293 (2005).
- <sup>19</sup>J. Li and Y. Kishimoto, *Phys. Plasmas* **12**, 054505 (2005).
- <sup>20</sup>T. Matsumoto, J. Li, and Y. Kishimoto, *Nucl. Fusion* **47**, 880 (2007).
- <sup>21</sup>W. Dorland and G. W. Hammett, *Phys. Fluids B* **5**, 812 (1993).
- <sup>22</sup>H. Sugama, T.-H. Watanabe, and W. Horton, *Phys. Plasmas* **14**, 079902 (2007).
- <sup>23</sup>M. Nakata, T.-H. Watanabe, H. Sugama, and W. Horton, *Phys. Plasmas* **17**, 042306 (2010).
- <sup>24</sup>F. Jenko, *Phys. Lett. A* **351**, 417 (2006).
- <sup>25</sup>P. N. Guzdar, R. G. Kleva, and L. Chen, *Phys. Plasmas* **8**, 459 (2001).
- <sup>26</sup>L. Chen, Z. Lin, and R. B. White, *Phys. Plasmas* **7**, 3129 (2000).
- <sup>27</sup>G. Manfredi, C. M. Roach, and R. O. Dendy, *Plasma Phys. Controlled Fusion* **43**, 825 (2001).
- <sup>28</sup>D. H. E. Dubin, J. Krommes, C. Oberman, and W. W. Lee, *Phys. Fluids* **26**, 3524 (1983).
- <sup>29</sup>J. Anderson, J. Li, and Y. Kishimoto, *Phys. Plasmas* **14**, 082313 (2007).
- <sup>30</sup>P. N. Guzdar, R. G. Kleva, A. Das, and P. K. Kaw, *Phys. Plasmas* **8**, 3907 (2001).
- <sup>31</sup>L. Chen, Z. Lin, R. B. White, and F. Zonca, *Nucl. Fusion* **41**, 747 (2001).